

---

# A Dynamical Graph Prior for Relational Inference

---

**Liming Pan\***

School of Computer and Electronic Information  
Nanjing Normal University  
Nanjing, China 210046  
pan.liming@njnu.edu.cn

**Cheng Shi\* & Ivan Dokmanić<sup>†</sup>**

Departement Mathematik und Informatik  
Universität Basel  
Basel, Switzerland 4051  
{firstname.lastname}@unibas.ch

## Abstract

Relational inference aims to identify interactions between parts of a dynamical system from the observed dynamics. Current state-of-the-art methods fit a graph neural network (GNN) on a learnable graph to the dynamics. They use one-step message-passing GNNs—intuitively the right choice since non-locality of multi-step or spectral GNNs may confuse direct and indirect interactions. But the *effective* interaction graph depends on the sampling rate and it is rarely localized to direct neighbors, leading to local minima for the one-step model. In this work, we propose a *dynamical graph prior* (DYGR) for relational inference. The reason we call it a prior is that, contrary to established practice, it constructively uses error amplification in high-degree non-local polynomial filters to generate good gradients for graph learning. To deal with non-uniqueness, DYGR simultaneously fits a “shallow” one-step model with shared graph topology. Experiments show that DYGR reconstructs graphs far more accurately than earlier methods, with remarkable robustness to under-sampling. Since appropriate sampling rates for unknown dynamical systems are not known a priori, this robustness makes DYGR suitable for real applications in scientific machine learning.

## 1 Introduction

Understanding interactions is key to understanding the function of dynamical systems in physics [3], biology, neuroscience [14], epidemiology [24], sociology [5], to name a few. It is often time-consuming or even impossible to determine this structure experimentally: for example, neuronal connectivity is determined by painstaking analyses of electron microscopy images. On the other hand, there has been an explosion of availability of signal measurements. It is thus extremely attractive to devise methods which determine interactions from the observed dynamics alone.

The seminal work on neural relational inference (NRI) [17] showed that in some cases graph neural networks (GNNs) can perform well on this challenge [17]. GNN-based methods use a graph generator and a dynamics learner<sup>3</sup>: the graph generator produces a candidate graph while the dynamics learner tries to match the dynamics to data, acting as a surrogate for the original system. Since the dynamics of a node only depend on its neighbours it is intuitive to use a single-step message-passing GNN: multi-step message passing or spectral GNNs leverage may confuse direct and indirect neighbors. Indeed, single-step architectures appear in the original NRI work and its various adaptations [2; 20; 12; 13; 36; 34].

An implicit assumption in a single-step scheme is that the sampling rate is sufficiently high. With a low sampling rate the effective interaction graph is non-local which causes a single-step surrogate

---

\*Equal contribution.

<sup>†</sup>To whom correspondence should be addressed.

<sup>3</sup>Even when called differently, these two components can usually be identified.

to confuse direct and indirect interactions. Single-step message passing also limits the expressivity of neural surrogates. The vanilla GCN [18] and many other GNNs implicitly assume homophily and act as low-pass graph filters [35]. Although they can handle certain heterophilic data [21], a single-layer GNN can only implement a limited range of graph filters. With an unknown dynamical model, especially a nonlinear one, it is necessary to use a graph filter which is adaptive to data such as ChebyNet [8] and GPR-GNN [6] which use filters.

In this work, we propose a *dynamical graph prior* (DYGR) for relational inference. Our model simultaneously uses a high-degree non-local polynomial and a “shallow” adjacency matrix to approximate the effective interactions between consecutive state samples. The polynomial filter is sensitive to graph perturbations which generates good gradients for graph learning. As there are, in general, multiple graph matrices that can result in the same polynomial filters, we simultaneously fit a parallel single-step model which helps resolve the direct interactions but does not suffer from local minima thanks to the gradients from the polynomial model. Experiments show that DYGR achieves significantly higher inference accuracy than any of the earlier approaches. Notably, it finds the direct interactions even at very low sampling rates where earlier approaches severely degrade. Code available: <https://github.com/DaDaCheng/DYGR>.

## 1.1 Related Work

**Relational Inference.** Classical approaches to relational inference measure correlations [25], mutual information [32], transfer entropy [29] or causality [27] of system trajectories. These approaches cannot perform future state predictions. Other studies focus on relational inference with known dynamical models [31; 26]. These methods are often designed for particular dynamics. When only system trajectories are observed, a family of approaches fits symbolic expressions for the driving ODE from a library of basis function [4] together with inferring the graph. These methods require knowing or accurately approximating the derivatives, and their performance crucially relies on the chosen candidate function library. NRI [17] infers the interaction graph in an unsupervised way while simultaneously predicting the state evolution. The scope of NRI has been extended to dynamic graphs [12], graphs with heterogeneous interactions [13], modular meta-learning problems [2]. It has also found applications in learning protein interactions [36] and was adapted to make causal claims [20]. The model has been extended to the non-amortized setting, where the graph encoder is often removed [20; 34]. The dynamics learner part of these models is a GNN with one-step message passing.

**Spectral Graph Neural Networks.** Two basic design paradigms for GNNs are via graph (spatial) and spectral graph convolutions. “Spatial” graph convolution aggregates neighborhood information; spectral filters are generically non-local [23]. ChebyNet [8] parameterizes the convolution kernel by Chebyshev polynomials of the diagonal matrix of Laplacian eigenvalues. Two other GNNs that use polynomial graph filters are APPNP [11] and GPR-GNN [6]. By making the weights of matrix polynomials trainable, GPR-GNN can adaptively work as low-pass or high-pass graph filters. For relational inference problems, spatial GNNs are relatively more straightforward to preserve locality via one-step message-passing and thus have been widely considered in different methods.

## 1.2 Our Contributions

Contrary to prior belief, we show that relational inference by non-localized filters works much better when properly designed. While earlier work avoids direct–indirect confusion via one-step message-passing, it suffers from local minima even in the presence of weak indirect interactions which prevents it from fitting the dynamics. We experimentally show that a non-local model removes local minima in dynamics learning. To mitigate the ambiguity arising from rooting matrix polynomials, we run a single-step model in parallel, but now benefitting from good gradients from the multi-step model. In addition to better graphs we also get a much better model for the dynamics and thanks to the better landscape greatly reduce the number of samples required to learn the graph. At the level of engineering our model is similar to the original NRI model, but the performance boost this simple change brings about is remarkable across the board.

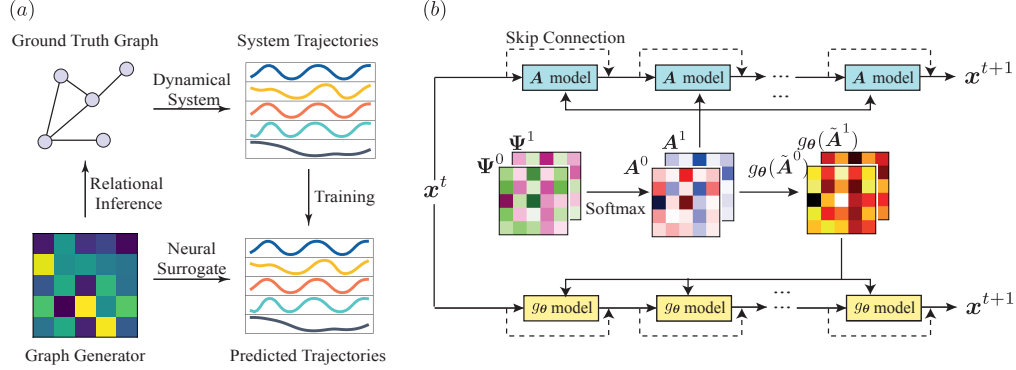


Figure 1: (a) An illustration of the relational inference problem. (b) The architecture of the full model. We train two dynamics surrogates with shared topology. The detailed architecture of  $\mathbf{A}$  model and  $g_\theta$  model can be found in Section 4.

## 2 Preliminaries

We consider a graph  $G = (V, E)$  on  $|V| = n$  vertices, which describes the interaction relations among components of a dynamical system. Let  $\mathbf{A}$  be the adjacency matrix,  $\tilde{\mathbf{A}} = \mathbf{D}^{-1/2}\mathbf{A}\mathbf{D}^{-1/2}$  its symmetric normalized version, and  $\tilde{\mathbf{L}} = \mathbf{I} - \mathbf{D}^{-1/2}\mathbf{A}\mathbf{D}^{-1/2}$  the symmetric normalized Laplacian. We use  $\mathbf{M}$  to denote a general graph matrix such as the adjacency matrix or the Laplacian.

### 2.1 Graph Dynamical Systems

Node  $i$  at time  $t$  is described by a state vector  $\mathbf{x}_i^t \in \mathbb{R}^{d_s}$ . We write  $\mathbf{x}^t = (\mathbf{x}_1^t, \mathbf{x}_2^t, \dots, \mathbf{x}_n^t)$  for the state of all nodes at time  $t$ . We consider both continuous- and discrete-time graph dynamical systems with synchronized updates,

$$\begin{array}{cc} \text{Continuous} & \text{Discrete} \\ \dot{\mathbf{x}}_i^t = f_i(\mathbf{x}_i^t, (\mathbf{x}_k^t)_{k \in N_i}) & \mathbf{x}_i^{t+1} = f_i(\mathbf{x}_i^t, (\mathbf{x}_k^t)_{k \in N_i}), \end{array} \quad (1)$$

where  $N_i$  is the set of vertex  $i$ 's neighbours and the dot denotes the time derivative. In relational inference the form of  $f_i$  for the dynamics and the interaction relations are both unknown. We observe some trajectories of the system and aim to infer the graph; see Figure 1(a) for an illustration.

### 2.2 Polynomial Graph Filters

A degree- $K$  polynomial graph filter with coefficients  $\boldsymbol{\theta} = (\theta_0, \dots, \theta_K)$  is defined as

$$g_\theta(\mathbf{M}) = \sum_{k=0}^K \theta_k \mathbf{M}^k.$$

Assuming  $\mathbf{M}$  is symmetric, we let  $\mathbf{M} = \mathbf{U}\boldsymbol{\Lambda}\mathbf{U}^\top$  be its eigenvalue decomposition. Then  $g_\theta(\mathbf{M}) = \mathbf{U}g_\theta(\boldsymbol{\Lambda})\mathbf{U}^\top$ , where  $g_\theta(\boldsymbol{\Lambda})$  applies element-wise to the diagonal elements of  $\boldsymbol{\Lambda}$  and  $g_\theta(\lambda) = \sum_{k=0}^K \theta_k \lambda^k$ . The scalar polynomial  $g_\theta(\lambda)$  is called the convolution kernel. By the Weierstrass approximation theorem, any continuous function on a bounded interval can be approximated by a polynomial with arbitrary precision.

## 3 Retrieving Interactions from the Effective Graph

### 3.1 Effective Interaction Graph

Unless the sampling rate is high, the effective graph modeled by the neural surrogate contains both direct and indirect interactions. Let us illustrate this. Consider a linear dynamics with scalar states.

Let  $\mathbf{x}^t = [x_1^t, \dots, x_n^t]^T$  be the vector of node states at time  $t$  and

$$\dot{\mathbf{x}}^t = \beta \mathbf{M} \mathbf{x}^t.$$

The states at  $t$  and  $t + \delta t$  are related as

$$\mathbf{x}^{t+\delta t} = \exp(\beta \mathbf{M} \delta t) \mathbf{x}^t,$$

where  $\exp(\beta \mathbf{M} \delta t)$  is the matrix exponential which encodes the effective interaction graph. Since

$$\exp(\beta \mathbf{M} \delta t) = \mathbf{I} + \beta \mathbf{M} \delta t + \frac{\beta^2}{2!} \mathbf{M}^2 \delta t^2 + \dots,$$

the interactions in principle exists instantaneously for all path-reachable nodes. For small  $\delta t$ , the power series can be approximated by truncating at first order in  $\delta t$  and the interaction graph is effectively encoded by  $\mathbf{M}$ , but for large  $\delta t$ , we need to include higher-order terms.

For general nonlinear dynamics let  $\bar{N}_i$  be the set of nodes that  $x_i^{t+\delta t}$  depends on. Let  $q_i$  be the effective transition function,  $x_i^{t+\delta t} = q_i((x_k^t)_{k \in \bar{N}_i})$ . If  $q_i$  is continuous, Kolmogorov–Arnold theorem lets us write [16; 33]

$$x_i^{t+\delta t} = \rho_i \left( \sum_{j \in \bar{N}_i} J_{i,j} \phi(x_j^t) \right),$$

for some continuous  $\phi$  and  $\rho_i$ . The function  $\phi$  is independent of  $q_i$ , and the parameters  $\mathbf{J} = (J_{i,j})$  can be interpreted as interaction strengths. To build a neural surrogate for the effective system, we can approximate  $\phi$  and  $\rho_i$  by neural networks and identify the interaction strengths via training; the NRI decoder can be interpreted in this sense. NRI further distinguishes a node and its neighbours as  $x_i^{t+\delta t} = x_i^t + \rho(x_i, \sum_{j \in \bar{N}_i} A_{i,j} \phi(x_i^t, x_j^t))$ , where  $\rho$  and  $\phi$  are neural networks and  $\mathbf{A} = (A_{i,j})$  trainable parameters.

While neural networks may approximate the effective dynamics, the inferred matrix  $\mathbf{A}$  is (at best) close to the *effective* interaction graph  $\mathbf{J}$ , rather than the true adjacency. In a linear system the effective graph is generated by a polynomial of the transition matrix which motivates the following *polynomial* neural surrogate:

$$x_i^{t+\delta t} = x_i^t + \rho \left( x_i, \sum_{j \in \bar{N}_i} g_{\theta}(\mathbf{A})_{ij} \phi(x_i^t, x_j^t) \right).$$

We will show that this surrogate benefits relational inference in both linear and nonlinear cases. In the following, we discuss (i) when then effective interaction graph can confuse direct and indirect interactions, and (ii) when and how a polynomial neural surrogate can helps to set things straight.

### 3.2 Effect of Observation Intervals

To what extent the effective interaction graph reflects the direct interactions is determined by the intrinsic properties of dynamics and by the sampling interval  $\delta t$ . In this section we empirically study the effect of the sampling rate in two cases where the effective graph can be determined exactly: continuous-time linear dynamics  $\dot{\mathbf{x}}^t = \beta \mathbf{A} \mathbf{x}^t$  where the effective interaction graph is  $\mathbf{J} = \exp(\beta \mathbf{A} \delta t)$ , and a discrete-time linear system with synchronized updates  $\mathbf{x}^{t+1} = \tilde{\mathbf{A}} \mathbf{x}^t$  where the effective graph is  $\tilde{\mathbf{A}}^{\delta t}$ . We compare the true graph defined by  $\mathbf{A}$  with the effective graph  $\mathbf{J}$  by plotting the AUC as a function of  $\delta t$  in Figure 2.

There is a qualitative distinction between the continuous and discrete systems, but in both performance deteriorates as  $\delta t$  grows. For continuous dynamics, the AUC remains close to 100% for small  $\beta T$ , meaning that the effective graph is dominated by direct interactions. When  $\beta T$  becomes larger,

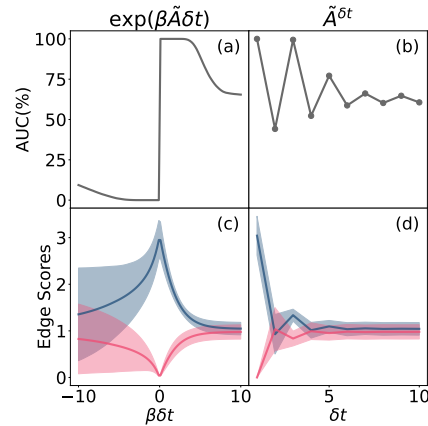


Figure 2: Effects of observation intervals on the effective interaction graph. The AUC for (a) linear (a) continuous and (b) discrete dynamics. The absolute value of normalized average score for (c) continuous and (d) discrete dynamics. The shaded regions show the standard deviation of each edge class. The results are obtained on an Erdős–Rényi graph with  $n = 30$  and  $p = 0.3$ .

direct–indirect confusion deteriorates performance. The average scores for positive and negative classes become closer even for small  $\beta T$ . This signifies a loss of stability which makes it more likely to misclassify edges.

For discrete dynamics, odd hops results in a larger AUC, which leads to the perhaps counter-intuitive conclusion that larger observation intervals do not always yield worse relational inference. Intuitively, there is always a length-3 walk between two directly connected nodes  $i, j$  as  $i \rightarrow j \rightarrow i \rightarrow j$ , but we can find a length-2 walk between only when they share a common neighbour. The general trend is still that large observation intervals result in a direct–indirect confusion.

From these two examples, we can loosely categorize sampled dynamics into (i) those where the effective interaction graph is strongly correlated with direct interactions and (ii) those where coarse sampling severely obfuscates direct interactions. In Section 5, we show experimentally that for different sampling rates many well-known dynamical models belong to the first class.

### 3.3 Interaction Graph Retrieval and Noise Amplifier Effect of Graph Polynomials

Even if we can find the *effective* interaction graph (which is the best we can hope for without additional assumptions) and this graph is correlated with the true adjacency, the question is how to recover the direct interactions. We discuss this issue in cases where the effective graph is either strongly or weakly correlated with the direct interactions.

First, we consider a weakly correlated example. Consider a linear system where the effective graph is a polynomial of  $\mathbf{M}$  with coefficients  $\theta^*$ ,  $\mathbf{J} = g_{\theta^*}(\mathbf{M})$ . Suppose we find  $\mathbf{J}$  and now want to find  $\mathbf{M}$ ; we thus need to solve  $g_{\theta'}(\mathbf{M}') \approx \mathbf{J}$  for  $\mathbf{M}$  and  $\theta$ . But the solution of  $g_{\theta'}(\mathbf{M}') \approx \mathbf{J}$  is in general not unique even when we know the polynomial coefficients  $\theta$ . If  $\mathbf{J} = \mathbf{M}^2$ , the matrix square root equation  $(\mathbf{M}')^2 = \mathbf{J}$  is solved by  $\mathbf{U}\text{diag}(\mu_1, \dots, \mu_n)\mathbf{U}^\top$ , where  $\mu_i = \pm\sqrt{\lambda_i}$ . In order to identify the correct sign pattern we need to use additional prior knowledge about the graph, such as sparsity. In Appendix A, we show that for a general polynomial with known  $\theta$  the solution is unique only when the convolution kernel  $g_{\theta}(\lambda)$  is injective (for example, the matrix exponential) and the graph matrix has no repeated eigenvalues. When  $\theta$  is not known, the number of solutions becomes much larger (we always have the trivial solution  $\theta'_i = \delta_{i,1}$  and  $\mathbf{M}' = \mathbf{J}$ ).

In the strongly correlated case, the interaction graph is close to the direct interaction graph in the sense that positive and negative edges can be classified. While the equation  $g_{\theta'}(\mathbf{M}') \approx \mathbf{J}$  may still have many solutions we only want to build a binary classifier which is possible directly from the effective graph. This means that single-step message passing may suffice. However, as we show experimentally in Section 5, even weak indirect interactions trap this architecture in poor local minima. We now discuss how error amplification in polynomial filters solves the problem.

In a graph dynamical system  $x_i^{t+\delta t} = x_i^t + \rho(x_i, \sum_{j \in N_i} M_{i,j} \phi(x_i^t, x_j^t))$ , changing the value of  $M_{i,j}$  only affects the next state of node  $i$ ,  $x_i^{t+\delta t}$ . It means that errors in the learned interactions only generate gradients locally on the graph. But if we approximate the effective interaction graph by a polynomial,

$$g_{\theta}(\mathbf{M}) = \sum_{k=0}^K \theta_k \mathbf{M}^k \approx \mathbf{J}, \quad (2)$$

then a perturbation in  $M_{i,j}$  propagates through several hops, generating large loss for multiple nodes and thus removing local minima. The issue is that, while (2) can always be solved (consider the trivial assignment  $\theta_k = \delta_{k,1}$ ,  $\mathbf{M} = \mathbf{J}$ ), the solution does not necessarily correspond to the direct interaction graph.

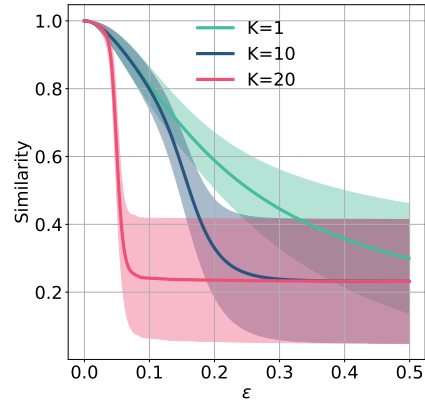


Figure 3: The noise amplifier effect of graph polynomials for relational inference. The results are obtained on an Erdős–Rényi graph with  $n = 50$  and  $p = 0.1$ .

Before we show how to address this issue in Section 4, let us demonstrate experimentally how including higher-order terms can make the model more sensitive to errors in the graph and produce better gradients. Let the ground truth graph filter be  $g_\theta(\tilde{\mathbf{A}}) = \tilde{\mathbf{A}}$  and consider a polynomial approximation  $g_{\theta'}$  with  $\theta'_1 = 1$ , and all higher order coefficients of order  $n^{-1}$ . Then the error  $\|g_{\theta'}(\tilde{\mathbf{A}})\mathbf{x} - g_\theta(\tilde{\mathbf{A}})\mathbf{x}\|_2$  is also of order  $n^{-1}$  and the small coefficients barely change the filtered signal. However, when  $\tilde{\mathbf{A}}$  is perturbed, the small coefficients amplify the perturbation. We interpolate between the  $\tilde{\mathbf{A}}$  and uniform random noise  $\Xi$  as  $\tilde{\mathbf{A}}_\epsilon = (1 - \epsilon)\tilde{\mathbf{A}} + \epsilon\Xi$  and plot the cosine similarity between  $\tilde{\mathbf{A}}\mathbf{x}$  and  $\tilde{\mathbf{A}}_\epsilon\mathbf{x}$  in Figure 3: the similarity decays rapidly when increasing  $K$ .

## 4 Dynamical Graph Prior for Relational Inference

**Graph Generator** We now introduce the full architecture of DYGR. We consider the non-amortized setting without an encoder [20]. We use a simple generator where the probability of an edge  $(i, j)$  is

$$A_{i,j}^a = (\text{Softmax}(\beta[\Psi_{i,j}^0, \Psi_{i,j}^1]))_a \text{ for } a \in \{0, 1\}, \quad (3)$$

$\Psi_{i,j}^0, \Psi_{i,j}^1 \in \mathbb{R}$  are trainable latent variables, and  $\beta$  is the inverse temperature.

**Neural Dynamics Surrogate** We generate two probability matrices,  $\mathbf{A}^{(a)}$  for  $a \in \{0, 1\}$  and the corresponding (probabilistic) graph filters  $\mathbf{F}^{(a)} = g_\theta(\tilde{\mathbf{A}}^{(a)})$ , where as before  $\tilde{\mathbf{A}}^{(a)}$  is the symmetric normalized version of  $\mathbf{A}^{(a)}$ , and the filter coefficients  $\theta$  are trainable. The dynamics surrogate predicts the next state as

$$\tilde{\mathbf{h}}_{(i,j)}^t = \sum_{a \in \{0,1\}} F_{i,j}^a \tilde{f}_e^a(\mathbf{x}_i^t, \mathbf{x}_j^t), \quad \mathbf{x}_j^{t+1} = \mathbf{x}_j^t + \tilde{f}_v \left( \sum_{i \neq j} \tilde{\mathbf{h}}_{i,j}^t \right). \quad (4)$$

In the above architecture,  $\tilde{f}_e^a$  are edge-wise MLPs, and  $\tilde{f}_v$  is a vertex-wise MLP. As explained in the previous section, a polynomial filter removes the local minima generated by indirect interactions, but it cannot guarantee that the learned  $\mathbf{A}$  is close to direct interactions since the roots of the matrix polynomial are not unique. Therefore, we simultaneously train another parallel dynamics neural surrogate using only the adjacency matrix, i.e., replacing  $F_{i,j}^a$  by  $A_{i,j}^a$  in Equation (4). The loss is simply the sum of MSEs of each neural surrogate. This strategy encourages the solution to stay close to the ground truth interactions while also leveraging the error amplification from graph polynomials. The overall architecture of the proposed model is shown in Figure 1(b). We call the model in Equation 4 using the adjacency matrix as  $\mathbf{A}$  model, and the model using a polynomial graph filter as  $g_\theta$  model. The two models work in parallel with shared  $\mathbf{A}$ .

### 4.1 Application to stochastic dynamics (fMRI)

We further show that with appropriate modifications DYGR can be adapted to work with stochastic systems such as functional brain region dynamics in fMRI. Indeed, with an addition of temporal smoothing it performs considerably better than a single-step model and as well as the state-of-the-art method based on mutual information, but unlike that method we learn a model for the dynamics. Using multiple  $\mathbf{A}$ - or  $g_\theta$ -models and deeper GNNs further improves performance. We leave a more detailed analysis of stochastic dynamics for future work.

## 5 Experiments

We consider several representative graph dynamical systems for validating the proposed algorithm. The dynamical systems include five continuous-time systems as the following. (i) Michaelis–Menten kinetics[15], a model for gene regulation circuits. (ii) Rössler oscillators [28] on graphs, which can generate chaotic dynamics. (iii) Diffusion, a continuous-time linear dynamics. (iv) Spring model that describes particles connected by springs and interacts via Hooke’s law; (v) Kuramoto model [19] that describes phase-coupled oscillators placed on a graph. We also consider two discrete-time dynamics as the following. (vi) Friedkin-Johnsen dynamics [9], a classical model for describing opinion formation [1; 22], polarization and filter bubble [7] in social networks; (vii) The coupled map network (CMN) [10], a discrete-time model with chaotic behavior. Moreover, we consider a

Table 1: Interaction graph inference accuracy measured by AUC and for various dynamical systems and inferring models. The results for NRI and DYGR are averaged over 10 independent runs. ER- $n$  or BA- $n$  denotes the name and number of nodes of the graph and  $\delta t$  denotes the sampling interval. The sampling interval refers to second-time samplings in pre-generated trajectories, not samplings during solving the ODEs. In the VOLUME column,  $a \times b$  corresponds to #trajectories  $\times$  #sampled steps. Boldface marks the highest accuracy.

MODEL	GRAPH	$\delta t$	VOLUME	MI	TE	NRI	DYGR
<b>MICHAELIS</b>	ER-50	1	$50 \times 10$	77.84	53.66	54.09 $\pm$ 2.22	<b>98.31<math>\pm</math>1.41</b>
		4	$50 \times 10$	55.93	51.95	51.85 $\pm$ 0.97	<b>88.66<math>\pm</math>8.73</b>
<b>MENTEN</b>	BA-50	1	$50 \times 10$	88.04	63.96	55.20 $\pm$ 1.81	<b>93.02<math>\pm</math>3.94</b>
		4	$50 \times 10$	50.18	60.30	52.26 $\pm$ 1.23	<b>87.42<math>\pm</math>6.08</b>
<b>RÖSSLER</b> <b>OSCILLATORS</b>	ER-50	1	$50 \times 10$	50.65	54.17	60.35 $\pm$ 4.58	<b>99.89<math>\pm</math>0.23</b>
		4	$50 \times 10$	52.28	54.13	51.95 $\pm$ 1.28	<b>56.82<math>\pm</math>3.56</b>
	BA-50	1	$50 \times 10$	56.28	62.64	59.81 $\pm$ 5.74	<b>90.55<math>\pm</math>16.13</b>
		4	$50 \times 10$	50.46	52.63	52.42 $\pm$ 1.76	<b>59.22<math>\pm</math>5.24</b>
<b>DIFFUSION</b>	ER-50	1	$20 \times 10$	56.00	57.63	70.66 $\pm$ 7.80	<b>93.44<math>\pm</math>4.87</b>
		4	$20 \times 10$	71.28	68.99	60.23 $\pm$ 6.73	<b>93.39<math>\pm</math>4.87</b>
	BA-50	1	$20 \times 10$	72.06	61.71	72.03 $\pm$ 11.62	<b>94.41<math>\pm</math>3.23</b>
		4	$20 \times 10$	86.38	69.77	59.01 $\pm$ 5.73	<b>90.55<math>\pm</math>5.14</b>
<b>SPRING</b>	ER-50	20	$15 \times 10$	72.24	76.05	99.84 $\pm$ 0.47	<b>99.99<math>\pm</math>0.02</b>
		60	$15 \times 10$	71.43	69.17	97.47 $\pm$ 2.93	<b>98.96<math>\pm</math>1.25</b>
	BA-50	20	$15 \times 10$	91.16	84.67	98.17 $\pm$ 5.40	<b>99.88<math>\pm</math>0.36</b>
		40	$15 \times 10$	<b>92.82</b>	63.67	67.89 $\pm$ 9.89	83.77 $\pm$ 9.14
<b>KURAMOTO</b>	ER-50	1	$30 \times 30$	64.69	64.76	82.09 $\pm$ 19.14	<b>94.93<math>\pm</math>12.94</b>
		4	$30 \times 30$	75.34	63.53	95.96 $\pm$ 5.01	<b>99.30<math>\pm</math>1.67</b>
	BA-50	1	$20 \times 30$	55.46	61.87	69.70 $\pm$ 18.16	<b>90.13<math>\pm</math>12.38</b>
		4	$20 \times 30$	51.13	64.62	89.57 $\pm$ 11.69	<b>97.48<math>\pm</math>2.78</b>
<b>FJ</b>	ER-50	1	$20 \times 10$	53.66	83.64	97.67 $\pm$ 1.06	<b>99.82<math>\pm</math>0.47</b>
		4	$20 \times 10$	58.98	59.00	65.25 $\pm$ 11.98	<b>75.48<math>\pm</math>10.60</b>
	BA-50	1	$20 \times 10$	52.32	86.88	91.62 $\pm$ 4.67	<b>92.63<math>\pm</math>13.46</b>
		4	$20 \times 10$	50.90	67.13	67.27 $\pm$ 9.59	<b>73.89<math>\pm</math>9.84</b>
<b>CMN</b>	ER-50	1	$20 \times 10$	87.39	64.35	89.76 $\pm$ 2.59	<b>97.58<math>\pm</math>3.38</b>
		4	$20 \times 10$	93.13	74.08	89.94 $\pm$ 1.42	<b>98.40<math>\pm</math>1.92</b>
	BA-50	1	$20 \times 10$	87.84	71.51	83.35 $\pm$ 2.30	<b>88.83<math>\pm</math>6.19</b>
		4	$20 \times 10$	92.28	75.39	83.05 $\pm$ 2.35	<b>92.97<math>\pm</math>5.26</b>
<b>NETSIM</b>	-	1	$5 \times 200$	94.73	74.83	71.57 $\pm$ 1.57	<b>95.09<math>\pm</math>0.68</b>
		2	$5 \times 100$	94.10	50.20	65.90 $\pm$ 6.24	<b>94.70<math>\pm</math>0.16</b>

public available dataset (viii) Netsim [30], a simulated fMRI data. A more detailed introduction of the dynamics and details in generating the data can be found in Appendix B.1.

## 5.1 Results on Relational Inference

We introduce several baseline methods that are included in the experiments. The first baseline is NRI. The original NRI is designed for the amortized setting where the trajectories do not share the underlying graph. As we mainly consider the classical non-amortized case, we use the version of NRI without a graph encoder [20]. Besides, we consider two statistical approaches, which are Mutual Information (MI) and Transfer Entropy (TE). More implementation details of the baselines can be found in Appendix B.2. The hyperparameters for DYGR are summarized in Appendix B.3. As Equation 4 is permutation invariant to the edge types  $a \in \{0, 1\}$ , it is possible that the learned corresponds to the complement graph of direct interactions. The graph/complement graph ambiguity is discussed in Appendix B.4.

We apply DYGR to the simulated systems and compare it to the baselines. We conduct experiments on Erdős-Rényi (ER) and Barabási-Albert (BA) graphs of different sizes and measure the interaction recovery accuracy by AUC. Table 1 summarises the average AUC with standard deviations. In

Table 1, the first four columns describe the dynamical model, graph type, sampling rate and data volume, respectively. As both NRI and DYGR can reach higher accuracy with increasing data volume, the volume of data in Table 1 is determined by the rough criterion that DYGR reaches above 90 AUC in the short sampling interval case. The data volumes are kept the same when increasing the sampling interval.

For the considered models, DYGR significantly improves the baseline methods. For example, in the Michaelis–Menten model, DYGR reaches good accuracy when the other baselines cannot recover helpful information on interaction relations (with an AUC of about 50.00). DYGR shows remarkable robustness to under-sampling. For example, for the Spring model in BA-50, while NRI and DYGR generate accurate predictions with small sampling intervals, DYGR degrades much less when increasing the sampling interval. The improvement is not limited to the large sampling rate case, as the error amplifier mechanism of the polynomial filter still works in this case. A phenomenon worth noticing is that the results generally display large fluctuations, which suggests that the loss landscape has many poor local minima. Using a polynomial filter helps escape these poor minima and improves the inference accuracy. In Appendix C.1, we further study the dependence of model performance on the polynomial order  $K$ . In Appendix C.2, we perform ablation studies to show that using only the polynomial filter is insufficient to generate stable predictions, as, in general, multiple graph matrices can result in the same polynomial filters. An interesting phenomenon is that a “good” graph for predicting the dynamics turn out to be close to the true graph. We further verify that the true graph is a local attractor for our model in Appendix C.3.

## 5.2 Robustness to Sampling Rate and Data Volume

We further explore the dependence of DYGR’s performance on sampling rates and data volume. For the discrete-time linear dynamics  $x^{t+1} = \tilde{\mathbf{A}}x^t$ , the effective interaction graph is highly uncorrelated with direct interaction graph  $\tilde{\mathbf{A}}$  when sampled at even intervals. We further apply relational inference algorithms to verify this phenomenon. The results are shown in Figure 4. The results from the explicit effective interaction graph  $\tilde{\mathbf{A}}^{\delta t}$  are shown by the gray dashed line. As expected, with the sampling with even intervals, both DYGR and the other three baselines fail to recover the direct interactions in this strongly-confused case. To retrieve the direct interaction graph, we need to impose further constraints, such as sparsity, on the graph.

The results from  $\tilde{\mathbf{A}}^{\delta t}$  provide a rough upper bound for the inference accuracy if we only use the effective interactions as the prediction. Both DYGR and the other three baselines are below this line, which suggests that even when some positive edges are, in principle, distinguishable, the algorithms can still not find them. The discrepancy between the rough upper bound and algorithm results is significantly more significant when  $\delta t$  is increased (for odd  $\delta t$ ). For example, when  $\delta t = 3$ , the bound is approximately 100 and is close to the  $\delta t = 1$  case; however, both NRI and DYGR deviate more from the bound for the former case. Nonetheless, DYGR is still closest to the rough bound for all sampling rates.

For continuous-time dynamics, we consider the Michaelis-Menten model as an example. We increase the sampling interval  $\delta t$  while keeping the volume of data fixed. The results for different methods are shown in Figure 5 (a). In general, the AUC decreases with  $\delta t$  for all the algorithms, which suggests that direct and indirect interactions can be more easily confused at larger sampling intervals. Still, DYGR shows more robustness to the sampling rates.

We further test the dependence on data volume and increase the data volume by including more training trajectories. The results are shown in Figure 5 (b). DYGR performs best for all different data volumes. It is also less sensitive to data volume and generates accurate predictions for small data volumes. The results overall show that DYGR works at much lower data volumes and sampling rates which may be essential in real applications where samples are hard or expensive to get.

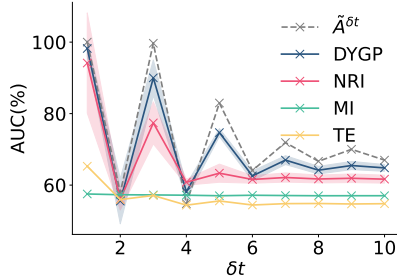


Figure 4: AUC versus sampling rate  $\delta t$ . The gray dashed line denotes the results from explicit interaction graph. For all the experiments, we keep the volume of training data ( $\#\text{trajectories} \times \#\text{sampled steps}$ ) identical. The results are obtained in ER-30 with data volume  $30 \times 20$ .



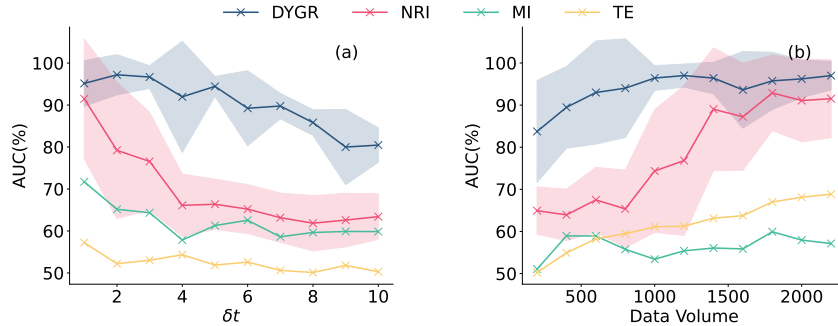


Figure 5: (a) AUC versus sampling rate  $\delta t$  and (b) AUC versus the data volume. The experiments are performed on an ER-20 graph. In (a), the data volume is fixed with a volume of  $50 \times 10$ . In (b), the trajectory length and sampling interval are fixed by 10 and 5. We increase the data volume by including more trajectories.

## 6 Discussion

The experiments show that in a broad range of qualitatively diverse dynamical systems and for a broad range of sampling rates, the non-local neural surrogate in DYGR indeed induces a favorable inductive bias and removes poor local minima that cause problems for the earlier local models. As a result, DYGR achieves state-of-the-art performance across the board, often by a large margin and at much lower data volumes.

We considered a setting where all trajectories share the same graph but our model can be extended to the amortized setting by using a graph encoder which preserves permutation invariance. The proposed model could also be adapted to make causal claims by using only the adjacency part at test time, as was done in [20].

Although we have incorporated polynomial filters to address the non-local interactions induced by coarse temporal sampling, DYGR works in the case where the effective interaction graph is strongly correlated with the direct interaction graph. This seems to be the case for all combinations of dynamics and sampling rates we tested, but a more challenging task is to look at the strongly mixed case where there is only a weak correlation between the effective and the true graph. This will likely require building new classes of graph priors for relational inference.

### Acknowledgments

LP would like to acknowledge support from National Natural Science Foundation of China under Grand No. 62006122 and 42230406. CS and ID were supported by the European Research Council (ERC) Starting Grant 852821—SWING.

### References

- [1] R. Abebe, J. Kleinberg, D. Parkes, and C. E. Tsourakakis. Opinion dynamics with varying susceptibility to persuasion. In *Proceedings of the 24th ACM SIGKDD International Conference on Knowledge Discovery & Data Mining*, pages 1089–1098, 2018.
- [2] F. Alet, E. Weng, T. Lozano-Pérez, and L. P. Kaelbling. Neural relational inference with fast modular meta-learning. *Advances in Neural Information Processing Systems*, 32, 2019.
- [3] A. Arenas, A. Díaz-Guilera, J. Kurths, Y. Moreno, and C. Zhou. Synchronization in complex networks. *Physics Reports*, 469(3):93–153, 2008.
- [4] J. Casadiego, M. Nitzan, S. Hallerberg, and M. Timme. Model-free inference of direct network interactions from nonlinear collective dynamics. *Nature Communications*, 8(1):1–10, 2017.
- [5] C. Castellano, S. Fortunato, and V. Loreto. Statistical physics of social dynamics. *Reviews of Modern Physics*, 81(2):591, 2009.

- [6] E. Chien, J. Peng, P. Li, and O. Milenkovic. Adaptive universal generalized pagerank graph neural network. In *International Conference on Learning Representations*, 2021.
- [7] U. Chitra and C. Musco. Analyzing the impact of filter bubbles on social network polarization. In *Proceedings of the 13th International Conference on Web Search and Data Mining*, pages 115–123, 2020.
- [8] M. Defferrard, X. Bresson, and P. Vandergheynst. Convolutional neural networks on graphs with fast localized spectral filtering. In *Proceedings of the 30th International Conference on Neural Information Processing Systems*, pages 3844–3852, 2016.
- [9] N. E. Friedkin and E. C. Johnsen. Social influence and opinions. *Journal of Mathematical Sociology*, 15(3-4):193–206, 1990.
- [10] P. Garcia, A. Parravano, M. Cosenza, J. Jiménez, and A. Marcano. Coupled map networks as communication schemes. *Physical Review E*, 65(4):045201, 2002.
- [11] J. Gasteiger, A. Bojchevski, and S. Günnemann. Predict then propagate: Graph neural networks meet personalized pagerank. In *International Conference on Learning Representations*, 2018.
- [12] C. Graber and A. Schwing. Dynamic neural relational inference for forecasting trajectories. In *Proceedings of the IEEE/CVF Conference on Computer Vision and Pattern Recognition Workshops*, pages 1018–1019, 2020.
- [13] S. Ha and H. Jeong. Learning heterogeneous interaction strengths by trajectory prediction with graph neural network. In *International Conference on Learning Representations*, 2023.
- [14] E. M. Izhikevich. *Dynamical systems in neuroscience*. MIT press, 2007.
- [15] G. Karlebach and R. Shamir. Modelling and analysis of gene regulatory networks. *Nature Reviews Molecular Cell Biology*, 9(10):770–780, 2008.
- [16] B. A. Khesin and S. L. Tabachnikov. *ARNOLD: Swimming Against the Tide: Swimming Against the Tide*, volume 86. American Mathematical Society, 2014.
- [17] T. Kipf, E. Fetaya, K.-C. Wang, M. Welling, and R. Zemel. Neural relational inference for interacting systems. In *International Conference on Machine Learning*, pages 2688–2697. PMLR, 2018.
- [18] T. N. Kipf and M. Welling. Semi-supervised classification with graph convolutional networks. In *International Conference on Learning Representations*, 2017.
- [19] Y. Kuramoto. Self-entrainment of a population of coupled non-linear oscillators. In *International Symposium on Mathematical Problems in Theoretical Physics: January 23–29, 1975, Kyoto University, Kyoto/Japan*, pages 420–422. Springer, 1975.
- [20] S. Löwe, D. Madras, R. Zemel, and M. Welling. Amortized causal discovery: Learning to infer causal graphs from time-series data. In *Conference on Causal Learning and Reasoning*, pages 509–525. PMLR, 2022.
- [21] Y. Ma, X. Liu, N. Shah, and J. Tang. Is homophily a necessity for graph neural networks? In *International Conference on Learning Representations*, 2022.
- [22] M. Okawa and T. Iwata. Predicting opinion dynamics via sociologically-informed neural networks. In *Proceedings of the 28th ACM SIGKDD Conference on Knowledge Discovery and Data Mining*, pages 1306–1316, 2022.
- [23] A. Ortega, P. Frossard, J. Kovačević, J. M. Moura, and P. Vandergheynst. Graph signal processing: Overview, challenges, and applications. *Proceedings of the IEEE*, 106(5):808–828, 2018.
- [24] R. Pastor-Satorras, C. Castellano, P. Van Mieghem, and A. Vespignani. Epidemic processes in complex networks. *Reviews of Modern Physics*, 87(3):925, 2015.

- [25] J. Peng, P. Wang, N. Zhou, and J. Zhu. Partial correlation estimation by joint sparse regression models. *Journal of the American Statistical Association*, 104(486):735–746, 2009.
- [26] J. Pouget-Abadie and T. Horel. Inferring graphs from cascades: A sparse recovery framework. In *International Conference on Machine Learning*, pages 977–986. PMLR, 2015.
- [27] C. J. Quinn, T. P. Coleman, N. Kiyavash, and N. G. Hatsopoulos. Estimating the directed information to infer causal relationships in ensemble neural spike train recordings. *Journal of Computational Neuroscience*, 30(1):17–44, 2011.
- [28] O. E. Rössler. An equation for continuous chaos. *Physics Letters A*, 57(5):397–398, 1976.
- [29] T. Schreiber. Measuring information transfer. *Physical Review Letters*, 85(2):461, 2000.
- [30] S. M. Smith, K. L. Miller, G. Salimi-Khorshidi, M. Webster, C. F. Beckmann, T. E. Nichols, J. D. Ramsey, and M. W. Woolrich. Network modelling methods for fmri. *Neuroimage*, 54(2): 875–891, 2011.
- [31] W.-X. Wang, Y.-C. Lai, and C. Grebogi. Data based identification and prediction of nonlinear and complex dynamical systems. *Physics Reports*, 644:1–76, 2016.
- [32] T. Wu, T. Breuel, M. Skuhersky, and J. Kautz. Discovering nonlinear relations with minimum predictive information regularization. *arXiv preprint arXiv:2001.01885*, 2020.
- [33] M. Zaheer, S. Kottur, S. Ravanbakhsh, B. Poczos, R. R. Salakhutdinov, and A. J. Smola. Deep sets. *Advances in Neural Information Processing Systems*, 30, 2017.
- [34] Y. Zhang, Y. Guo, Z. Zhang, M. Chen, S. Wang, and J. Zhang. Universal framework for reconstructing complex networks and node dynamics from discrete or continuous dynamics data. *Physical Review E*, 106(3):034315, 2022.
- [35] J. Zhu, Y. Yan, L. Zhao, M. Heimann, L. Akoglu, and D. Koutra. Beyond homophily in graph neural networks: Current limitations and effective designs. *Advances in Neural Information Processing Systems*, 33:7793–7804, 2020.
- [36] J. Zhu, J. Wang, W. Han, and D. Xu. Neural relational inference to learn long-range allosteric interactions in proteins from molecular dynamics simulations. *Nature Communications*, 13(1): 1–16, 2022.

## A Graph Retrieval

**Lemma A.1.** *Let the  $g_\theta : \mathbb{R} \rightarrow \mathbb{R}$  be a polynomial convolution kernel, and  $s_i$  be the number of real roots of  $g_\theta(x) - g_\theta(\lambda_i) = 0$ . If (i) the graph matrix  $\mathbf{M}$  is symmetric with distinct nonzero eigenvalues  $\{\lambda_1, \lambda_2, \dots, \lambda_n\}$ ; and (ii) if the convolution kernel  $g_\theta$  is injective, i.e.,  $s_i = 1$  for all  $\lambda_i$ , and  $g_\theta(x) \neq 0$  for  $x \neq 0$ , then the matrix equation  $g_\theta(\mathbf{M}') = g_\theta(\mathbf{M})$  has unique solution has unique solution  $\mathbf{M}' = \mathbf{M}$ . Otherwise, it has at least  $\prod_{i=1}^n s_i$  solutions.*

*Proof.* As  $g_\theta(\mathbf{M}')$  is a polynomial, then  $\mathbf{M}'$  and  $g_\theta(\mathbf{M}')$  commutes; therefore  $\mathbf{M}'$  and  $g_\theta(\mathbf{M})$  commutes as  $g_\theta(\mathbf{M}') = g_\theta(\mathbf{M})$ . Then  $\mathbf{M}'$  and  $g_\theta(\mathbf{M})$  can be simultaneously diagonalized. When  $\mathbf{M}$  has distinct nonzero eigenvalues and  $g_\theta$  is injective and  $g_\theta(x) \neq 0$  for  $x \neq 0$ , then also  $g(\mathbf{M})$  has distinct nonzero eigenvalues. In this case, the simultaneously diagonalizable basis for  $\mathbf{M}'$  and  $g(\mathbf{M})$  is unique (up to basis permutations), which is the eigenbasis  $\mathbf{U}$  of  $\mathbf{M}$ . Let the diagonal matrix of  $\mathbf{M}$  and  $\mathbf{M}'$  be  $\mathbf{\Lambda}$  and  $\mathbf{\Lambda}'$ , respectively. Then we have the equation  $\mathbf{U}g_\theta(\mathbf{\Lambda})\mathbf{U}^\top = \mathbf{U}g_\theta(\mathbf{\Lambda}')\mathbf{U}^\top$ . Equating the diagonal entries gives  $g_\theta(\lambda_i) - g_\theta(\lambda'_i) = 0$ . If  $g_\theta$  is injective, then the equation implies  $\lambda_i = \lambda'_i$ , and the solution is unique with  $\mathbf{A} = \mathbf{A}'$ .

If  $g_\theta$  is not injective, or the graph matrix  $\mathbf{M}$  itself has repeated eigenvalues, then  $g_\theta(\mathbf{M})$  could have repeated eigenvalues, and the diagonalizable basis can be non-unique, and the eigenbasis  $\mathbf{U}$  can be only one of them. For the eigenbasis, the equation  $g(\lambda_i) - g(\lambda'_i) = 0$  has  $s_i$  solutions. Pick any of the  $s_i$  solutions for each  $i$  gives a solution to the matrix equation  $g(\mathbf{M}') = g(\mathbf{M})$ , so there are  $\prod_{i=1}^n s_i$  solutions. Therefore, there are at least  $\prod_{i=1}^n s_i$  solutions.  $\square$

## B Experiment Details

### B.1 Dynamical Models and Data Generation

The detailed setups in generating the dataset is summarized in this Appendix. For all experiments, we set the number of validation trajectories to be 10. The sampling interval and the number of sampled trajectories are identical to the training set. The number of sampled trajectories and time steps are shown in Table 1 in the main text. All trajectories are normalized to  $[-1, 1]$  before feed into training for NRI and DYGR. In Table 1, for ER graphs the connection probability of is set to be 0.1, and for BA graphs, each new node is connected to  $m = 2$  existing nodes.

**Michaelis-Menten Kinetics** Michaelis–Menten kinetics [15] describes enzymatic reaction kinetics. The node state  $x_i$  is one-dimensional, which describes concentrations of molecular species. Its evolution reads

$$\dot{x}_i = -x_i + \frac{1}{|N_i|} \sum_{j \in N_i} \frac{x_j}{1 + x_j},$$

The equation is integrated with an ODE solver, and the step size is set to be  $\delta t = 1$ .

**Rössler Oscillators** Rössler Oscillators [28] is a three-dimensional dynamical system composed of one nonlinear and two linear equations. The model has been extended to graphs, where each node carries a Rössler Oscillator that are coupled through the edges. The model has been used to study synchronization in power grids and neuron oscillations. The state  $x_i$  of each node is three-dimensional, where the evolution[4] reads:

$$\begin{aligned} \dot{x}_{i,1} &= -x_{i,2} - x_{i,3} + \frac{1}{|N_i|} \sum_{j \in N_i} \sin(x_{j,1}), \\ \dot{x}_{i,2} &= x_{i,1} + 0.1x_{i,2}, \\ \dot{x}_{i,3} &= 0.1 + x_{i,3}(x_{i,3} - 18). \end{aligned}$$

When integrating the model, we set  $\delta t = 1$ .

**Diffusion.** The graph diffusion equation is  $\dot{x} = \tilde{\mathbf{L}}x$ . We use the scale Laplacian  $\mathbf{I} - \tilde{\mathbf{L}}$  and set  $\delta t = 0.1$ .

**Springs model.** The springs model describes particles connected by springs and interact via Hooke’s law. The model was considered in NRI for testing the algorithm. We use the same setup as NRI,

where particles are confined in a 2D box with elastic boundaries, and each particle is described by the location  $\mathbf{r}_i \in \mathbb{R}^2$  and velocity  $\mathbf{v}_i \in \mathbb{R}^2$ . The system’s ODE reads

$$\frac{d\mathbf{r}_i}{dt} = \mathbf{v}_i, \quad \frac{d\mathbf{v}_i}{dt} = -k \sum_{j \in N_i} (\mathbf{r}_i - \mathbf{r}_j). \quad (5)$$

We use the trajectories of  $\mathbf{r}_i$  and  $\mathbf{v}_i$  as observed data. The size of the box is set to be 5. We use the code for simulating the springs model provided by NRI<sup>4</sup>. The initial locations are sampled as i.i.d. Gaussians  $\mathcal{N}(0, 0.5)$ , and the initial velocities is a random vector of norm 0.5. Newton’s equation of motion is integrated with a step size of 0.001 and then subsamples each 100 step to get the training and testing trajectories. Each sampled trajectory contains 49 snapshots of the system states.

**Kuramoto model.** Kuramoto model [19] describes phase-coupled oscillators placed on a graph. For the model, each vertex  $i$  has a phase  $\phi_i$ , whose evolution is described by the following ODE

$$\frac{d\phi_i}{dt} = \omega_i + k \sum_{j \in N_i} \sin(\phi_j - \phi_i), \quad (6)$$

where  $\omega_i$  are the intrinsic frequencies and  $k$  is the coupling strength. We use the implementation and default parameters provided by Löwe et al.<sup>5</sup>. The observables contains  $d\phi_i/dt$ ,  $\sin \phi_i$ ,  $\phi_i$  and  $\omega_i$ . The sampling rate is  $\delta t = 0.01$ .

**Friedkin-Johnsen Dynamics.** The Friedkin-Johnsen (FJ) dynamics [9] is a classical model for describing opinion formation [1; 22], polarization and filter bubble [7] in social networks. In FJ model, each vertex at time  $t$  holds an “expressed” opinion  $x_i^t \in [-1, 1]$  and an internal opinion  $s_i \in [-1, 1]$ . While  $s_i$  does not change over time,  $x_i$  evolves according to the rule

$$x_i^{t+1} = \frac{s_i + \sum_{j \in N_i} x_j^t}{1 + |N_i|}, \quad (7)$$

where  $|N_i|$  is the degree of vertex  $i$ . The model reaches an equilibrium state in the long-time limit where all vertices hold a constant opinion. We study relational inference for the model in its transient state. We sample the initial expressed and internal opinions from a uniform distribution in  $[-1, 1]$  and update vertex states for some steps to generate the dataset. We take both  $s_i$  and  $x_i^t$  as observed quantities.

**Coupled Map Networks.** Coupled Map Networks [10] is a discrete-time system that can generate chaotic dynamics.

$$x_i^{t+1} = (1 - \epsilon)x_i^t + \frac{\epsilon}{|N_i|} \sum_{j \in N_i} f(x_j^t), \quad f(x_i^t) = \eta x_i^t(1 - x_i^t).$$

We set  $\epsilon = 0.2$  and  $\eta = 3.5$ . We use the implementation provided by Zhang et al.<sup>6</sup>.

**Netsim** Netsim [30] simulates blood-oxygen-level-dependent imaging data across different regions within the human brain. The interaction graph describes the directed connectivity between brain regions. The dataset volume is  $50 \times 200$ , and the graph has  $n = 15$  nodes. As in Löwe et al., we do not split the data into training/validation sets but use all the data in each phase.

## B.2 Baseline Methods and Implementation Details

**NRI.** NRI was originally designed in the amortized setting when each trajectory has a distinct interaction graph. It was extended to the non-amortized case for relational [34] and causal [20] inference. In the non-amortized setting, the graph encoder is not necessary. As we do not require make causal claims, we do not use the test-time adaption technique in Löwe et al., but infer the interaction graph during training time. The predicted interaction graph is picked through the MSE loss in a validation set. We re-implement NRI based on Löwe et al. for the non-amortized case with binary edge types, and use their default hyperparameters. More details can be found in our implementation available online.

<sup>4</sup><https://github.com/ethanfetaya/NRI>,

<sup>5</sup><https://github.com/loeweX/AmortizedCausalDiscovery>

<sup>6</sup><https://github.com/kby24/AIDD>

**Mutual Information (MI).** Mutual information of two random variables is defined as

$$MI_{i,j} = \sum_{x_i, x_j} P(x_i, x_j) \log \frac{P(x_i, x_j)}{P(x_i)P(x_j)}, \quad (8)$$

where  $P(x_i, x_j)$  is the joint distributions of  $x_i$  and  $x_j$  sampled from the system trajectories, and  $P(x_i)$  ( $P(x_j)$ ) are their marginals. The random variables are defined on each vertex for the relational inference problem. We compute the mutual information for all pairs of nodes, which is further taken as the score for the presence of an edge. The node state distributions are approximated from the sampled trajectories.

**Transfer Entropy (TE)** The transfer entropy is defined as

$$TE_{i,j} = H(x_j^t | x_j^{t-1}) - H(x_j^t | x_j^{t-1}, x_i^{t-1}),$$

where  $H(\cdot|\cdot)$  is the conditional entropy. In order to estimate the conditional entropy numerically, the observed trajectories are discretized by data binning. The number of bins is picked from  $\{2, 200\}$ , and we report the higher accuracy.

Unlike NRI and DYGR, MI and TE do not require a validation set. For a fair comparison, we compute MI and TE on the training and validation set combined. When there are multiple variables, we compute MI or TE for each variable and take the average as the prediction. We use the implementations from netrd package<sup>7</sup> for MI and TE.

### B.3 Hyperparameters for DYGR

All the results of DYGR reported in the main text (except the Netsim dataset) are obtained under identical neural network architecture and hyperparameters. We use Adam optimizer to train the model. The learning rate is set to be 0.1 for the graph generator and 0.0005 for the dynamics surrogate. The inverse temperature parameter  $\beta$  of the graph generator in Equation (3) of the main text is set to be 0.5. For all other datasets except Netsim, the polynomial filter is truncated at  $K = 4$ , and the number of GNN layers is set to 1.

The Netsim dataset is stochastic, and we introduce some addition techniques of temporal smoothing. In particular, we set  $k = 6$  with 4 GNN layers. In order to make the outputs in the first three hidden layers stable, we perform linear interpolation on consecutive data points and fit the hidden layers outputs to the interpolated data. In addition, we replace the data at each time step with the average on its neighbouring time steps. More details can be found in our implementation available online. We leave a more detailed analysis of stochastic dynamics for future work.

### B.4 Graph / Complement Graph Ambiguity

The neural surrogate essentially classify the edges into two types, but cannot determine which type correspond to the positive edges and which to the negative. In fact Equation 4 is permutation invariant to the edge-types  $a \in \{0, 1\}$ . Therefore, there is the graph/complement graph ambiguity problem. Moreover, the effective interaction graph itself can be negatively correlated to the adjacency matrix. For example, for the linear ODE  $\dot{x} = \beta \tilde{\mathbf{A}}x$ , a negative  $\beta$  makes the effective interaction negatively correlated with the interaction graph, as shown in Figure 2. In practical applications, we can use sparsity prior, or compare with the statistical methods to decide which one as the prediction. In Table 1, we simply report  $\max\{\text{AUC}, 1-\text{AUC}\}$ .

## C More Results

### C.1 Dependency on Polynomial Orders

We take the Michaelis-Menten Kinetics as an example to test the dependency on the polynomial order  $K$ . We consider an ER graph with  $n = 20$  nodes and generate the trajectories at sampling interval  $\delta t = 4$ . The volume of training/validation/test data are  $50 \times 10/10 \times 10/10 \times 10$ , respectively. The training and test errors and graph inference AUC versus  $K$  are shown in Figure A1. The model performance is optimized at an intermediate value of  $K$ , which shows that including higher-order terms can help in recovering the interactions.

<sup>7</sup><https://netrd.readthedocs.io/en/latest/>

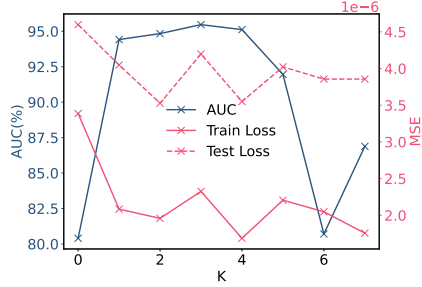


Figure A1: The dependency of model performance on polynomial order  $K$ . The results are averaged over 10 independent runs.

### C.2 Ablation Study of Using Only Polynomial filters

Our proposed model reduces to NRI if the polynomial filter part is removed. Therefore, the ablation study mainly focuses on the case when we only use a polynomial filter. As we have discussed in the main text, there are, in general, multiple graph matrices that can result in the same polynomial filters, so it is hard to control which one will converge. We use only the  $g_\theta$  model to verify the phenomenon and conduct experiments with different random seeds in Pytorch. We use the diffusion model as an example and record the predictions generated by  $\mathbf{A}$ ,  $\tilde{\mathbf{A}}$  and  $g_\theta(\tilde{\mathbf{A}})$  in Table A1. Any of these three matrices has predicted the interaction graph best under one random seed, suggesting that the convergence is hard to control if we only use the polynomial filter. As we only list three related graph matrices, other better matrices might not be included. Therefore, an  $\mathbf{A}$  model is necessary to stabilize the solutions.

Table A1: Interaction graph AUC when using only the polynomial model. The data volume is set to be  $20 \times 10$ . Each row corresponds to an independent run with a different random seed. Boldface marks highest accuracy.

MODEL	GRAPH	$T_o$	SEED	$\mathbf{A}$	$\tilde{\mathbf{A}}$	$g_\theta(\tilde{\mathbf{A}})$
<b>DIFFUSION</b>	ER-50	1	0	85.90	<b>92.04</b>	90.47
		1	1	80.74	87.92	<b>91.23</b>
		1	2	<b>93.86</b>	84.49	80.77
		1	3	87.79	<b>93.04</b>	90.86
	ER-50	4	0	<b>91.51</b>	86.89	80.21
		4	1	86.71	<b>87.07</b>	82.27
		4	2	<b>78.35</b>	70.96	66.95
		4	3	<b>85.50</b>	76.51	76.80

### C.3 Local Attractiveness of Ground Truth Graph

The experimental results show that the “good” graph for dynamics prediction is also correct. In other words, the true graph is an attractor (at least locally) when we make the graph trainable. We test the local attractiveness of the ground truth graph via the following experiment. In particular, we train the neural surrogate by keeping the graph fixed on each set of graphs. The set contains a ground truth graph as well as many distorted graphs. We randomly select a fraction of the edges for distortion and flip its edge type. We consider the Diffusion model and generate the training trajectories by simulating with the ground truth graph and train the neural surrogate on each graph for 10 times independently. The average train and test MSE error versus the proportion of distorted edges is shown in Figure A2. From Figure A2, for both NRI and DYGR, the train and test error in general increase with the proportion of distorted edges, which reflects that with the ground truth graph, we can better predict the dynamics.

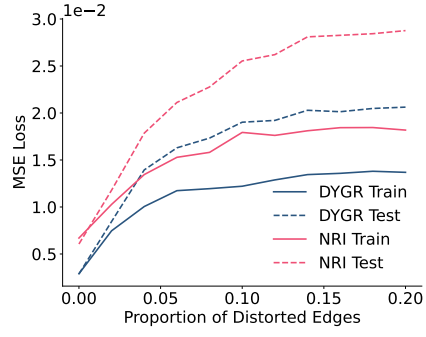


Figure A2: The training and test loss of neural surrogate with fixed graph. The graph is an ER graph with  $n = 20$  and  $p = 0.5$ , and the sampling interval is set to be  $\delta t = 1$ . The volume of training data is  $50 \times 10$ . We randomly flip a fraction of edges, and train the model on the fixed distorted graph.